SPATIOTEMPORAL SEISMIC HAZARD AND RISK ASSESSMENT OF M9.0 MEGATHRUST EARTHQUAKE SEQUENCES OF WOOD-FRAME HOUSES IN VICTORIA, BRITISH COLUMBIA, CANADA

Lizhong Zhang[1], Katsuichiro Goda[2,3], Maximilian J. Werner[4], and Solomon Tesfamariam[5]

[1]Department of Civil Engineering, University of Bristol, Bristol, United Kingdom
[2]Department of Earth Sciences, University of Western Ontario, London, Canada
[3]Department of Statistical & Actuarial Sciences, University of Western Ontario, London, Canada
[4]School of Earth Sciences and Cabot Institute, University of Bristol, Bristol, United Kingdom
[5]School of Engineering, The University of British Columbia, Kelowna, British Columbia, Canada

Megathrust earthquake sequences, comprising mainshocks and triggered aftershocks along the subduction interface and in the overriding crust, can impact multiple buildings and infrastructure in a city. The time between the mainshocks and aftershocks usually is too short to retrofit the structures; therefore, moderate-size aftershocks can cause additional damage. To have a better understanding of the impact of aftershocks on city-wide seismic risk assessment, a new simulation framework of spatiotemporal seismic hazard and risk assessment of future M9.0 sequences in the Cascadia subduction zone is developed. The simulation framework consists of an Epidemic Type Aftershock Sequence (ETAS) model, ground-motion model, and state-dependent seismic fragility model. The spatiotemporal ETAS model is modified to characterise aftershocks of large and anisotropic M9.0 mainshock ruptures. To account for damage accumulation of wood-frame houses due to aftershocks in Victoria, British Columbia, Canada, state-dependent fragility curves are implemented. The new simulation framework can be used for quasi-real-time aftershock hazard and risk assessments and city-wide post-event risk management.

KEYWORDS
Spatiotemporal ETAS seismicity model; Cascadia subduction earthquakes; Mainshock-aftershock sequences; State-dependent aftershock fragility curves; Wood-frame houses; City-wide seismic risk; Damage accumulation.

1 INTRODUCTION

Recent M9.0 earthquake sequences, such as the 2004 Aceh-Andaman earthquake, the 2010 Maule earthquake, and 2011 Tohoku earthquake, triggered large aftershock events (e.g., M≥7.0) on the subduction interface and in the overriding crust, demonstrating the destructive effects of aftershocks on buildings [1,2]. Because the time to repair damaged buildings between a mainshock and aftershocks is often short, the cumulative damage effect of buildings due to aftershocks can have a significant impact on post-earthquake risk assessment [3–5]. A spatiotemporal seismic risk assessment that considers the cumulative damage effect due to M9.0 earthquake sequences is necessary to quantify the impact of aftershocks on post-event risk management decision-making, including resource allocation, evacuation planning, and rapid seismic loss estimation [6,7].

Devastating M9.0 events are not limited to the most active seismic regions mentioned above and could occur in other subduction zones. For example, according to turbidite records of the past 10,000 years, the Cascadia subduction zone (CSZ) ruptured 19 times [8]. The current best estimate of the mean recurrence period for M9.0 events in the CSZ is 526 years, and the last event occurred in 1700 [9]. On the other hand, Ventura *et al.* [10] estimated that 56% of buildings in British Columbia (BC), Canada, are wood-frame houses, 40% of which were built before 1970. Since seismic provisions of the National Building Code of Canada were adopted and enforced in BC after 1973, the seismic resistance of old residential houses is likely to be below the current seismic standard of the building stock in BC. Consequently, in the urban areas (e.g., Vancouver and Victoria) of BC, a large number of wood-frame houses [11] may be particularly at risk from M9.0 subduction earthquake sequences.

To conduct a spatiotemporal seismic risk assessment, a model that can describe the time-dependent seismicity rate in space and time is necessary. An epidemic type aftershock sequence (ETAS) model [12] is such a spatiotemporal seismicity model. The model has been employed to conduct operational earthquake loss forecasting in California and Italy [13,14]. All above-mentioned studies, however, focussed on shallow crustal seismicity, whereas regional spatiotemporal seismic risk assessments in subduction zones are rarely carried out. Recently, Zhang *et al*. [15] applied the ETAS model to subduction-zone regions and developed a new simulation framework to assess spatiotemporal seismic hazard and risk due to aftershocks triggered by M9.0 events. Their case study of Tohoku-like events has shown that synthetic catalogues from the new simulation framework are in good agreement with the observed M9.0 Tohoku sequence. Moreover, Zhang *et al*. [16] investigated the variability of ETAS parameters across different subduction-zone regions using global earthquake catalogues to derive preferred ETAS parameters for future M9.0 earthquake sequences. Their outputs allow forecasting spatiotemporal seismic hazard due to M9.0 sequences in subduction zones using observed catalogues in global subduction zones.

For seismic risk assessment, recent studies have investigated the seismic performance of individual buildings in western Canada when exposed to hypothetical M9.0 events in the CSZ [17–19]. For instance, Koduru and Haukaas [18] highlighted the significant contribution (up to 75%) of megathrust subduction events to the total monetary loss for the case of a single 15-storey high-rise building in Vancouver. In terms of the impact of aftershocks occurring in the CSZ on individual buildings, Salami and Goda [20] showed that mainshock-aftershock sequences can cause additional 5%-20% damage in comparison with mainshocks alone. On the other hand, megathrust earthquakes affect many buildings simultaneously. Therefore, city-wide seismic risk assessments were conducted to make decisions more efficiently for Vancouver and Victoria [11,21,22]. However, time-dependent seismic risk assessments of multiple buildings within a city subjected to M9.0 earthquake sequences in the CSZ have not been investigated. In addition, most spatiotemporal seismic risk studies ignore the cumulative damage effect due to aftershocks. This is because (1) a seismicity model to describe the mainshock-aftershock sequences in space and time is not available in the CSZ, and (2) state-dependent aftershock fragility curves are not available for various building typologies, and only mainshock fragility curves that do not account for the cumulative damage effect of aftershocks have been used. Recently, Zhang *et al.* [23] have developed state-dependent fragility curves of wood-frame houses in BC to estimate the damage state (DS) of wood-frame houses after each event during an earthquake sequence. The new state-dependent fragility curves can be combined with the quasi-real-time aftershock forecasting hazard assessment to build a simulation framework of city-wide spatiotemporal seismic hazard and risk due to megathrust subduction earthquake sequences in the CSZ.

This study, for the first time, assesses spatiotemporal seismic hazard and risk due to M9.0 mainshock-aftershock sequences using a realistic building portfolio of wood-frame houses in Victoria, BC, Canada. The developed spatiotemporal simulation framework is innovative, and its main novelty is attributed to the integration of two compatible components. The first component is the ETAS seismicity model for the CSZ. Unlike other active subduction zones, where many observed events are available to calibrate the ETAS parameters (e.g., Tohoku region, Japan), the CSZ lacks direct observations; thus, its ETAS parameters for M9.0 scenarios are calibrated based on seismicity data from other global subduction zones [16]. Secondly, the state-dependent aftershock fragility curves of wood-frame houses are used [23] to better estimate the cumulative damage effect of mainshock-aftershock sequences and to develop a real-time risk forecasting framework for decision-making. In addition, a realistic building dataset of wood-frame houses in Victoria is employed, aiming at estimating the total seismic loss for the building portfolio. The objectives of this paper are: 1) to show how the simulation framework of spatiotemporal seismic hazard and risk assessment, developed for active subduction regions, can be applied to the CSZ, 2) to quantify the impact of aftershocks on the short-term seismic risk assessment in terms of DS and seismic loss, and 3) to demonstrate how the outputs of the framework can be used for post-earthquake decision-making. In the following, **Section 2** describes the new framework of the spatiotemporal seismic hazard and risk assessment for Victoria. **Section 3** discusses the impact of mainshocks and aftershocks on the city-wide seismic risk assessment in Victoria.

2 SPATIOTEMPORAL SEISMIC HAZARD AND RISK ASSESSMENT IN VICTORIA

An overview of the framework of spatiotemporal seismic hazard and risk assessment is given in this section. The framework consists of a seismicity model (ETAS model), a ground motion model (GMPEs), and a seismic fragility model (aftershock fragility curves) as shown in **Figure 1**. Synthetic catalogues are generated from ETAS simulations. The synthetic catalogues contain the times, magnitudes, and locations of mainshock-aftershock sequence events. Subsequently, the synthetic catalogues and local soil conditions (V_{s30}) are used as inputs to GMPEs to estimate the ground motion intensity measures of the mainshock-aftershock sequences at different sites. Following that, the intensity measures at multiple sites are applied to the aftershock fragility curves to estimate the DSs and losses of multiple wood-frame houses at different times after a mainshock.

2.1 Seismicity model

This subsection analyses regional seismicity for the CSZ and introduces suitable ETAS parameters based on global subduction data. In **Section 2.1.1**, the Advanced National Seismic System (ANSS) (https://www.ncedc.org/anss/catalog-search.html) and the Seismic Hazard Earthquake Epicentre File (SHEEF) catalogues [24] are analysed to investigate the main characteristics of the regional seismicity for the CSZ, while ETAS simulations for the CSZ are presented in **Section 2.1.2**.

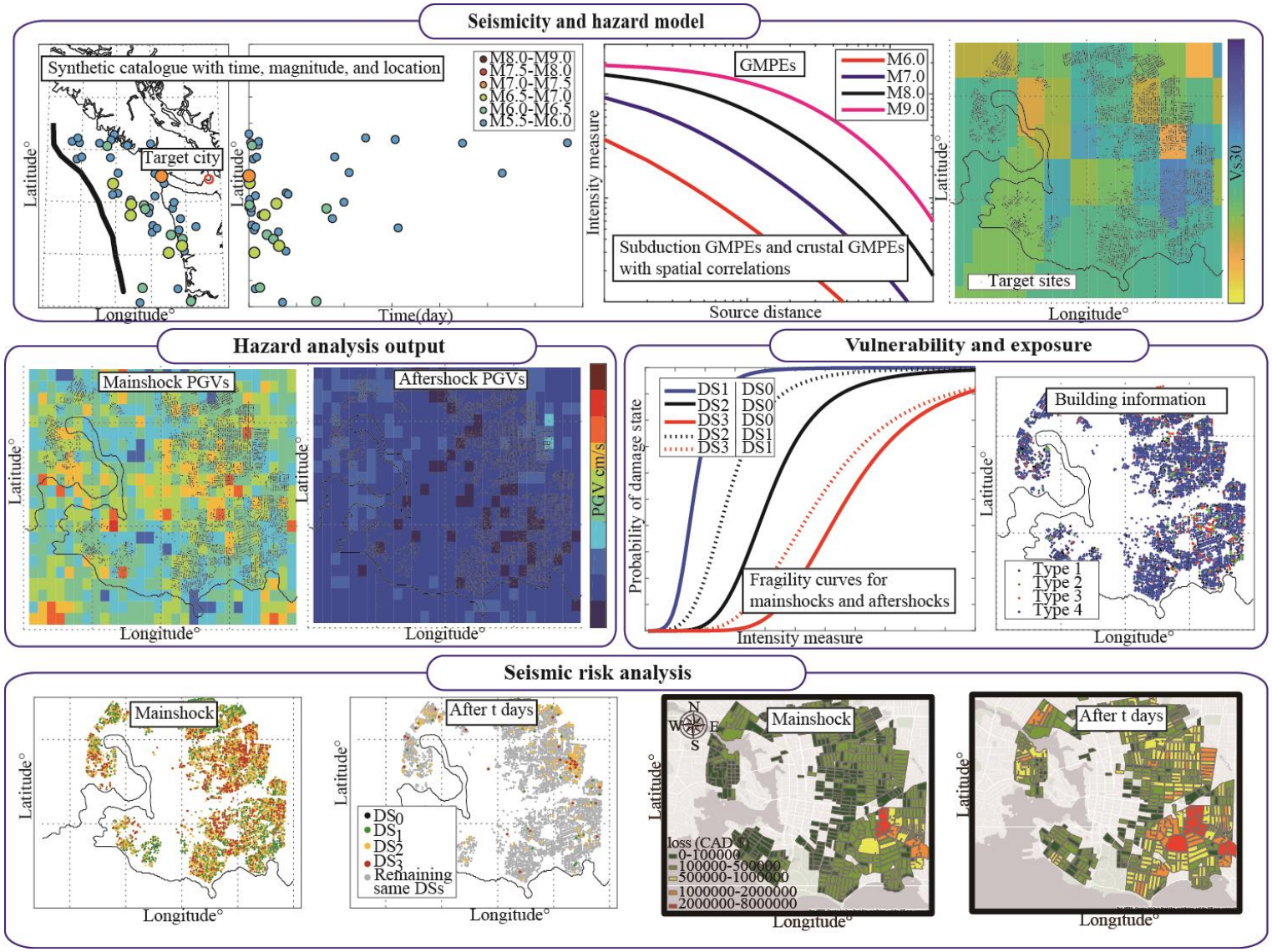

Figure 1. Simulation framework of spatiotemporal seismic hazard and risk assessments.

2.1.1 Analysis of ANSS and SHEEF catalogues in the CSZ

Although a small dataset of observed events in the CSZ does not allow calibrating the ETAS parameters reliably, *b*-value estimation is easier and important because the generic ETAS simulation framework assumes $b = 1.0$ [16]. The local ANSS and SHEEF databases are used to estimate the completeness magnitude M_c and *b*-value because they include more events than global catalogues (e.g., National Earthquake Information Centre). In addition, the SHEFF catalogue consists of a uniform magnitude type and revised earthquake hypocenters [24]. A shortcoming of the SHEFF catalogue is that only events in the vicinity of Canada until 2010 are available (e.g., seismicity data in Oregon are missing). We therefore search the ANSS catalogue for more events in a larger spatiotemporal window.

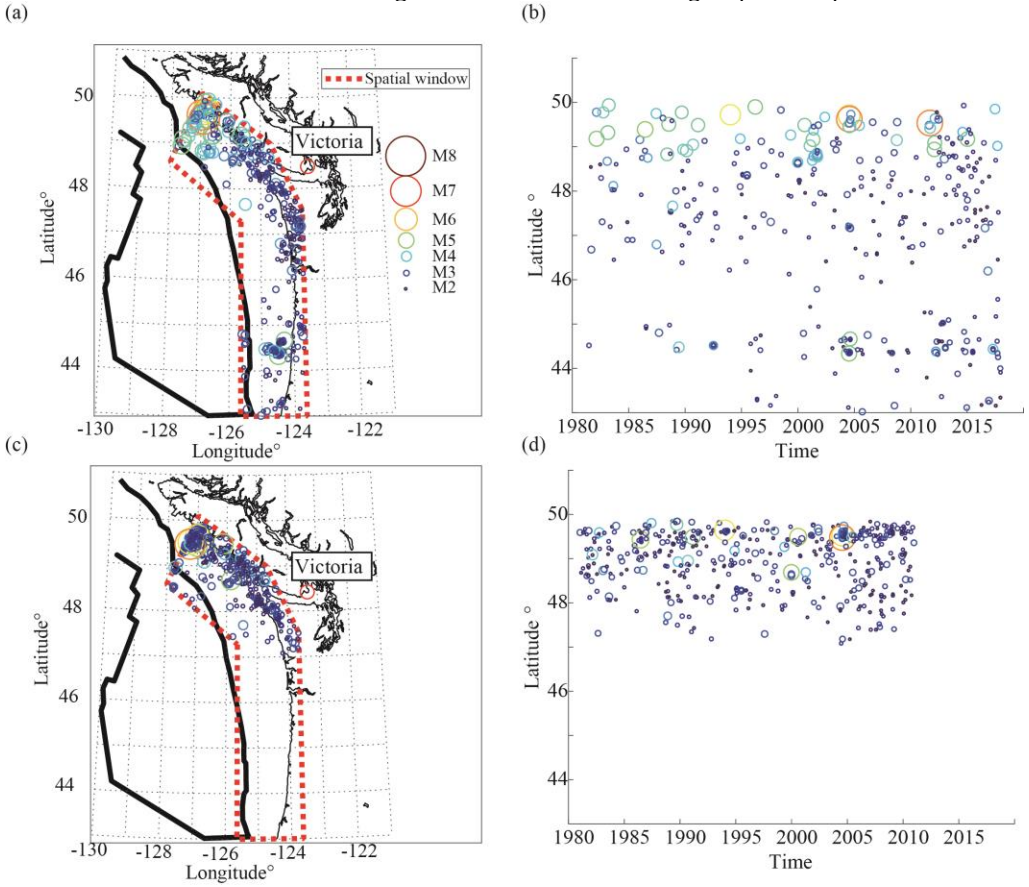

Figure 2. Seismicity of the CSZ in target window (dashed red polygon) listed in the ANSS catalogue during 1981-2017 (top) and the SHEEF catalogue during 1981-2010 (bottom): (a, c) epicentral locations and (b, d) latitudinal distribution over time.

Events are selected from the ANSS and SHEFF catalogues between 1 January 1981 and 31 December 2017 with depths less than 100 km. Following the 2014 U.S. national seismic hazard model [25], a spatial window is set as shown in **Figure 2**(a) by enclosing down-dip rupture limits of the M9.0 mainshock rupture model in the CSZ [26–28]; its eastern boundary extends to the western coastline of Vancouver Island. The southern edge of the target window is not extended into northern California (e.g., lower than 43°N), because some M7.0 events took place in the Mendocino Triple Junction rather than within the CSZ (e.g., the 2010 M6.5 Gorda Plate event and the 2014 M6.8 Ferndale event) [29]. **Figure 2** shows spatiotemporal plots of the observed events with M≥2.0 from the ANSS and SHEFF catalogues. The ANSS catalogue (**Figure 2**(b)) covers a larger area in the western coast of Washington and Oregon States and includes events after 2010. The SHEEF catalogue contains smaller events near 50° in latitude before 1990 as shown in **Figure 2**(d). These two sub-catalogues are used to estimate the *b*-values.

In **Figure 3**, the *b*-values of the CSZ based on the ANSS and SHEFF catalogues are estimated as 0.53±0.03 and 0.82±0.04, respectively. The *b*-value = 0.82 from the SHEFF catalogue suggests that the northern CSZ has a magnitude-frequency distribution more similar to other regions with *b*-value ≈ 1. The low *b*-value from the ANSS catalogue is due to missing events before 2000. Because of the fewer events in the CSZ (less than 100 with $M_{cut} = 4$), reliable estimates of the ETAS parameters cannot be obtained solely based on the local catalogues. ETAS estimation

(a prerequisite for modelling) requires well-recorded sequences [15]. Consequently, the global ETAS parameters (K_0 = 0.04±0.02, α = 2.3, c = 0.03±0.01, p = 1.21±0.08, γ =1.61±0.29, d = 23.48±18.17, and q = 1.68±0.55) with b-value=1.0 from Zhang *et al*. [16] for future M9.0 sequences are used to generate synthetic catalogues in the CSZ.

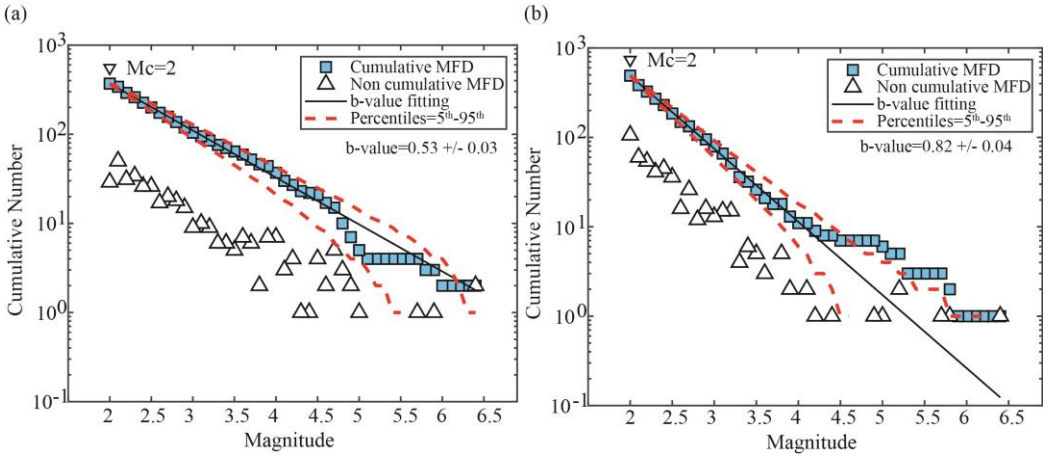

Figure 3. Observed magnitude–frequency distributions (MFD) and fitted Gutenberg–Richter laws with the maximum-likelihood estimates of the b-values and 5th–95th percentiles from (a) the ANSS and (b) the SHEFF catalogues.

2.1.2 ETAS simulation

The ETAS simulation framework with the anisotropic power-law kernel [15] is employed to generate synthetic catalogues of aftershocks given an M9.0 earthquake. The developed anisotropic power-law kernel combines the simulated 2D rupture rectangular area with a power-law beyond the rupture area, which can distribute the first generation of aftershocks anisotropically in space. However, in comparison with the bilateral rupture area of the Tohoku mainshock, several studies suggested a longer and narrower shape of the mainshock rupture area for the CSZ [25,30]. The M9.0 rupture dimensions of the CSZ are more similar to the 2004 M9.1 Aceh-Andaman earthquake, which has a greater rupture length-to-width ratio than the Tohoku mainshock [31]. In this study, the shape of the rupture area is developed and modelled by the down-dip edge models [26–28], and the rupture dimensions are simulated from the empirical scaling law [31]. The down-dip edge of the CSZ is critical for the hazard calculation, as it primarily controls the rupture distances from the mainshock to the coastal city (e.g., Victoria). Different down-dip edge models have been developed based on different assumptions of geothermal conditions, episodic tremor, and slip zones [28]. Rupture widths are simulated to capture the locations of different down-dip edge models from the 2014 USGS national seismic hazard model. In terms of the aftershock decay outside the CSZ rupture area, the same procedures as in the Tohoku case [15] are applied to build a spatial kernel function using 1D and 2D power laws. **Figure 4** shows the probability density distribution of the aftershock spatial distribution outside the rupture area of the M9.0 event with a rupture length of 1,100 km and width of 130 km.

Additional features including the depth, earthquake type, and focal mechanism, are assigned to each event in synthetic catalogues based on Zhang *et al*. [15]. These additional features allow simulating the rupture plane of large crustal and subduction-zone aftershocks (M≥6.5) and evaluating seismic intensity measures (IMs) using GMPEs. Depths for earthquakes with M<8 are sampled from empirical cumulative distribution functions (ECDFs) of depths obtained from past observations in the CSZ. The slab model [32] of the CSZ (**Figure 4**) is divided into sub-regions with 10 km width from the trench line to the continental crust to estimate the ECDFs of depth in each sub-region. We use past earthquakes M≥2 from the ANSS catalogue within the slab model. Events with depths less than 5 km are eliminated because the majority of these events are remote events, and their depths are poorly estimated with depths of 0 km [33].

All simulated earthquakes with M≥8 are treated as subduction-interface earthquakes, and the depths are assigned directly from the slab model [32] (**Figure 4**). Earthquake types (continental-crust, subduction plate-boundary, or subduction intra-plate) are defined by the sampled depths and the slab model. Earthquakes more than 20 km above the plate interface are defined as crustal events, earthquakes falling in the layer within ±20km of the plate interface are classified as subduction-interface events (allowing for depth uncertainty), and remaining deep earthquakes are treated as intra-slab events.

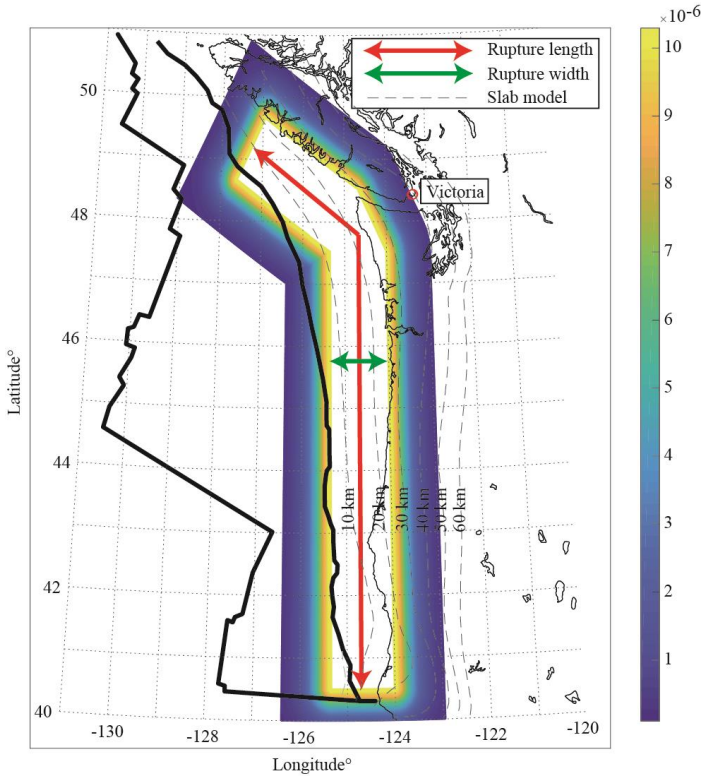

Figure 4. Probability density distribution of the aftershock spatial distribution outside a simulated rupture area of the M9.0 event (rupture length × rupture width = 1,100 km × 130 km).

Due to the plate motion of the subduction zone, the crustal and subduction-zone earthquakes tend to have similar strike directions as the subduction plane [15]. Following that, the strike and dip angles of the subduction and crustal aftershock are assumed to be similar to the strike and dip angles of the subduction plane. The ECDFs of strike and dip angles for crustal and subduction earthquakes are evaluated from the global Centroid Moment Tensor (gCMT) catalogue, and the sampled angles are assigned to the large aftershocks with M≥6.5. Specifically, given the target city is Victoria, the strike angle of a nodal plane 1 or 2 that is closer to the target strike angles (320°-350°) of the subduction plane of the northern and central CSZ is selected [32].

In total, 10,000 synthetic mainshock-aftershock catalogues are generated over a one-year period. The magnitude frequency distribution and the daily number of events in a squared root scale are shown in **Figure 5**. The aftershock seismicity rate with M≥5.5 is high immediately after the mainshock and gradually decays after day 5.

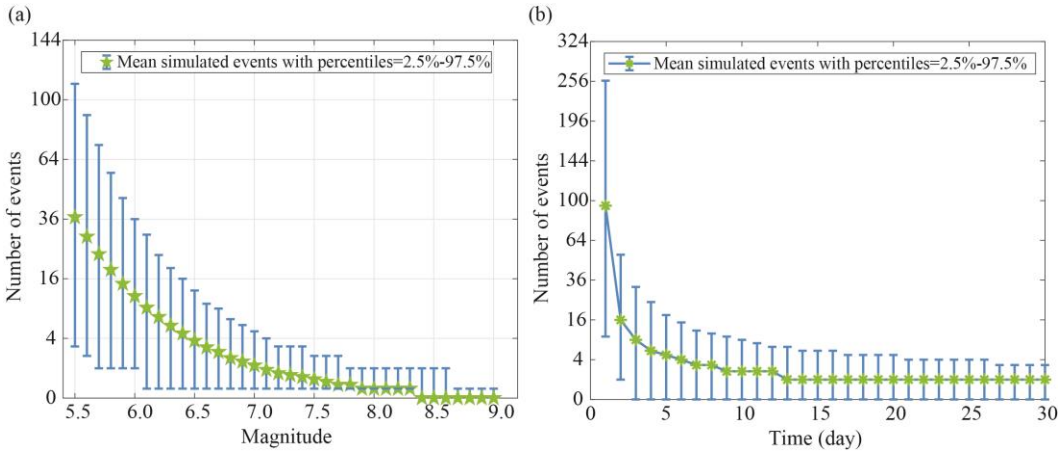

Figure 5. (a) Simulated magnitude-frequency distributions of aftershocks. (b) The daily number of simulated events over a month after the mainshock.

2.2 Ground motion model

To compute scenario-based shake maps of M9.0 earthquake sequences for the City of Victoria, the following GMPEs and V_{s30} information are used. PGV is adopted as IM in the risk analysis because PGV shows a better performance in capturing the cumulative damage effects of wood-frame houses [23]. Accordingly, the GMPEs by Ghofrani and Atkinson [34] and Boore *et al.* [35] are used to compute the PGV for subduction-zone and crustal earthquakes, respectively.

Ground motion models for the CSZ should reflect seismological findings from recent major subduction and crustal events. Although other global subduction-zone GMPEs are available (e.g., [36,37]), they do not include the ground motion from the 2011 Tohoku sequences, and thus the equations need to be extrapolated beyond the range of the underlying ground motion data. On the other hand, PGV is not always included as the output variable of the newest subduction-zone GMPEs [38,39]. Therefore, we use the GMPEs from Ghofrani and Atkinson [34], which includes the ground motion records from the 2011 Tohoku event together with adjustment factors for the CSZ to account for its deeper soil profile compared with Japan. In comparison with other crustal GMPEs from the NGA-West2, the GMPE by Boore *et al.* [35] requires less input information (e.g., unknown options for fault type and hanging wall effect). This is more suitable for southwestern BC, since a complete inventory of active faults and their geometry is not available, except for a few fault systems, such as the Leech River Valley fault [40].

The synthetic catalogues with times, magnitudes, locations, and earthquake types are applied to the GMPEs to calculate the median values of PGV. Source models for M≥6.5 crustal and subduction-zone aftershocks are generated from empirical scaling laws [31] and the ECDFs of strike and dip angles. This allows calculating the shortest rupture distances from the simulated rupture dimension to target sites.

The V_{s30} map of the City of Victoria is taken from Wald and Allen [41], and is generally consistent with the observations from Monahan and Levson [42]. The soil conditions in Victoria correspond to the National Earthquake Hazard Reduction Program site classes C to E (e.g., V_{s30} < 760 m/s). We use a grid size of 500 m × 500 m for the City of Victoria to produce the mainshock and aftershock shaking maps. We consider the spatial correlation models from Goda and Hong (2008) [43] and Goda and Atkinson (2010) [44] for crustal and subduction-zone events, respectively. The error terms are sampled from the inter-event sigma and the intra-event sigma with the spatial correlation models.

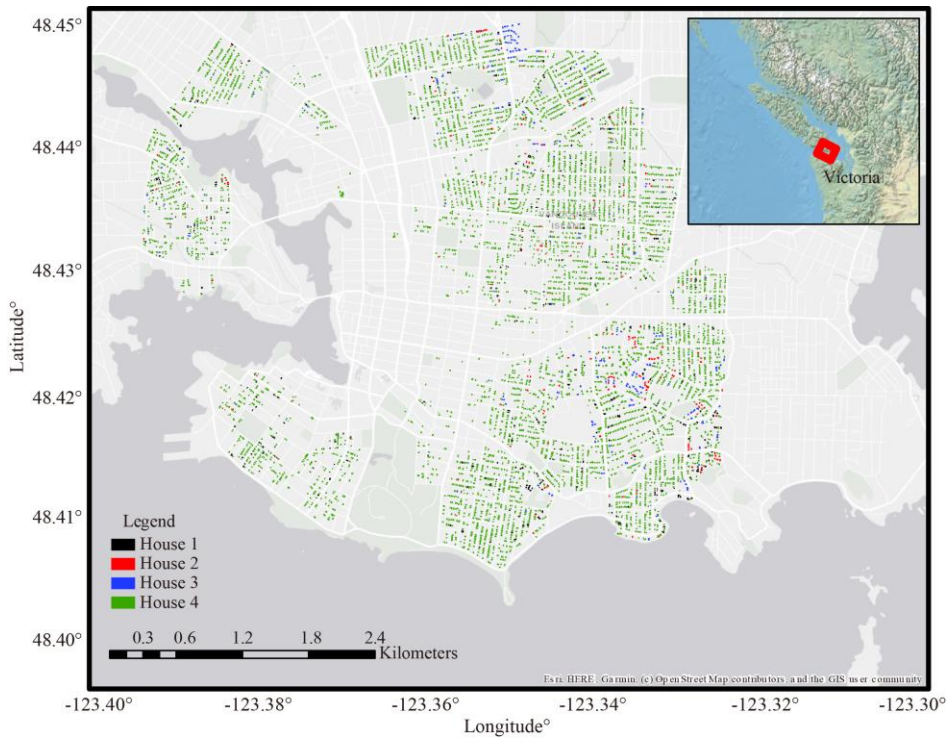

Figure 6. Spatial distribution of wood-frame houses in Victoria (6,711 in total with House 1 #387, House 2 #197, House 3 #257, and House 4 #5,870).

2.3 Seismic risk model

The state-dependent fragility curves of wood-frame houses [23] are used to assess the performance of the wood-frame houses under an M9.0 megathrust subduction earthquake sequence. To develop the state-dependent fragility curves, Zhang *et al*. [23] used structural responses before and after each event of real mainshock-aftershock records to obtain statistical relationships among the engineering demand parameter (EDP) prior to the seismic event, the intensity measure (IM) of the seismic event, and the EDP after the seismic event. The 3D dataset (pre-EDP-IM-post-EDP) is binned according to the same pre-DS. For each IM-post-EDP dataset that is classified by the same pre-DS, IM values corresponding to specific post-EDP intervals are then fitted to produce the state-dependent fragility curves. The developed fragility curves account for damage accumulation, providing the exceeding probability of DS given the IM of the event and the DS of the structure prior to the seismic excitation.

Due to different shear-wall configurations, four types of two-storey wood-frame houses are defined: (1) House 1 with stucco/engineered oriented strand board (OSB)/gypsum wallboard (GWB), (2) House 2 with engineered OSB/GWB, (3) House 3 with non-engineered OSB/GWB, and (4) House 4 with horizontal boards (shiplap)/GWB. The term 'engineered' for Houses 1 and 2 indicates that hold-downs and blocking of the wall panel are used to increase their seismic resistance and to meet the seismic code requirements [45]. By considering post-earthquake building inspections, three performance thresholds corresponding to Green, Yellow, and Red tags (hereafter referred to as DS_1, DS_2, and DS_3) are defined. Green tag (DS_1) represents a case where the house is inspected by a structural engineer and can be immediately occupied, Yellow tag (DS_2) indicates that access is limited except for professional maintenance, and Red tag (DS_3) means that the house is unsafe to occupy and requires retrofitting or rebuilding [46].

In total, 6,711 houses are considered for the seismic risk assessment in the City of Victoria. The building database is from BC assessment (https://www.bcassessment.ca/). From the building database, the following information was extracted: (1) location, (2) built year, (3) Actual Use by Category (AUC), and (4) building assessment value (Canadian dollars). We removed non-residual buildings and only considered single-family dwellings that are defined by AUC. To link the fragility curves of Houses 1-4 with individual houses in the building data, the wood-frame houses are classified into Houses 1-4 according to the construction years, which reflects expected seismic performances of the houses. The four different house types considered are: (1) House 1 - after 1991, (2) House 2 - from 1981 to 1990, (3) House 3 - from 1971-1980, and (4) House 4 - before 1970. The numbers of Houses 1-4 are 387, 197, 257, and 5,870, respectively. This is consistent with the descriptions from White and Ventura [45] that the majority of the wood-frame houses were built before 1973 and thus may be deficient in seismic capacity compared with the current seismic design standard in BC. **Figure 6** shows a plot of spatially distributed Houses 1-4 in Victoria.

To evaluate the seismic damage to each house, we interpolate the simulated PGVs of mainshock-aftershock shaking maps with 500 m × 500 m grid size linearly at each house location and apply the fragility curves. The total asset of the 6,711 houses is approximately $930 million Canadian dollars (CAD$). The seismic loss of the wood-frame houses is calculated based on the approach from Onur *et al.* [11]. Mean damage ratios of 5%, 40%, and 80% (slight, heavy, and major) are considered for Green (DS_1), Yellow (DS_2), and Red (DS_3) tags, respectively.

3 RESULTS AND DISCUSSION

This section discusses the impact of mainshocks and aftershocks from the CSZ on the municipality-wide seismic risk assessment in Victoria.

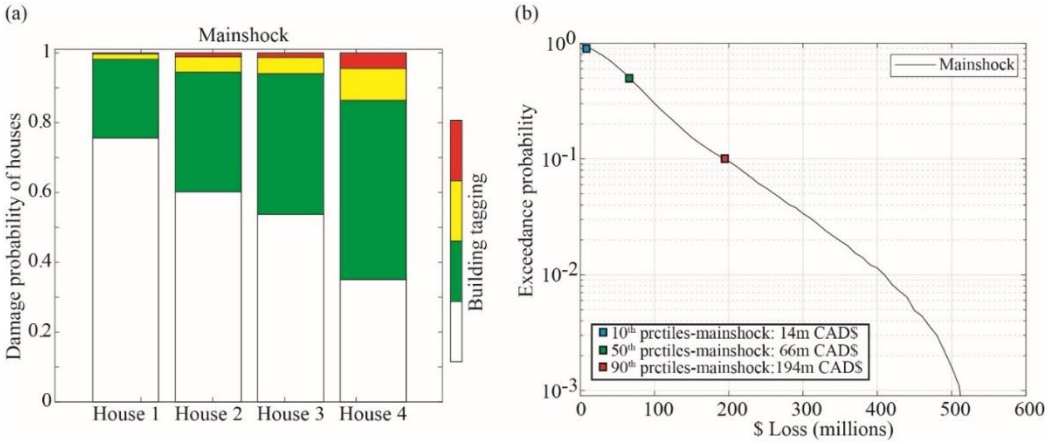

Figure 7. (a) Damage probability of Houses 1-4 after mainshocks based on 6,711 houses in Victoria. (b) Loss exceedance curves of mainshocks. 10th, 50th, and 90th percentiles of aggregated losses by mainshocks are 14, 66, and 194 million CAD$, respectively.

3.1 Impact of mainshocks on DS and seismic loss

The effects of the CSZ mainshocks on DS distributions and estimated seismic losses of the wood-frame houses are investigated in this subsection. **Figure 7** shows the damage probability of Houses 1-4 due to mainshocks only for the building portfolio of wood-frame houses (6,711 houses in total) in Victoria. House 4 makes up almost 90% of the wood-frame houses and is susceptible to significant damage. **Figure 7**(a) shows that the probabilities of DS_1, DS_2, and DS_3 right after the mainshocks are 51.3%, 9.2%, and 4.5%, respectively. Considering the total number of House 4 is 5,870, on average, 265 House 4 could change from DS_0 to DS_3 after the mainshocks. In **Figure 7**(b), the 10th, 50th, and 90th percentiles of total aggregated losses by the mainshocks are 14, 66, and 194 million CAD$, respectively. High estimated seismic losses (e.g., 500 million CAD$ with 0.001 exceedance probability) in the right tail in **Figure 7**(b) represent the effects of extreme IMs from the mainshocks. The large variability of PGV values of the mainshocks is due to two sources. The first source is the uncertainty of PGV from the GMPE [34]. The second source is the shortest distance from the mainshock rupture plane to Victoria, which depends on the down-dip edge models of the CSZ.

To visualise the uncertainty of the mainshocks from magnitude and rupture area on hazard analysis and quantify the impact of the mainshocks on risk assessment, single simulations of mainshock shaking maps, and DS and loss distributions corresponding to the 10th, 50th, and 90th percentiles of the total loss are examined closely. **Figure 8** shows the mainshock shaking maps corresponding to the 10th, 50th, and 90th percentiles of the total loss. The maximum and average PGV values of each shaking map are also indicated in **Figure 8**. The average PGV values of the 10th, 50th, and 90th percentile scenarios are 14, 25, and 44 cm/s, respectively, whereas the maximum PGV values of **Figure 8**(a)-(c) are 30, 52, and 90 cm/s, respectively.

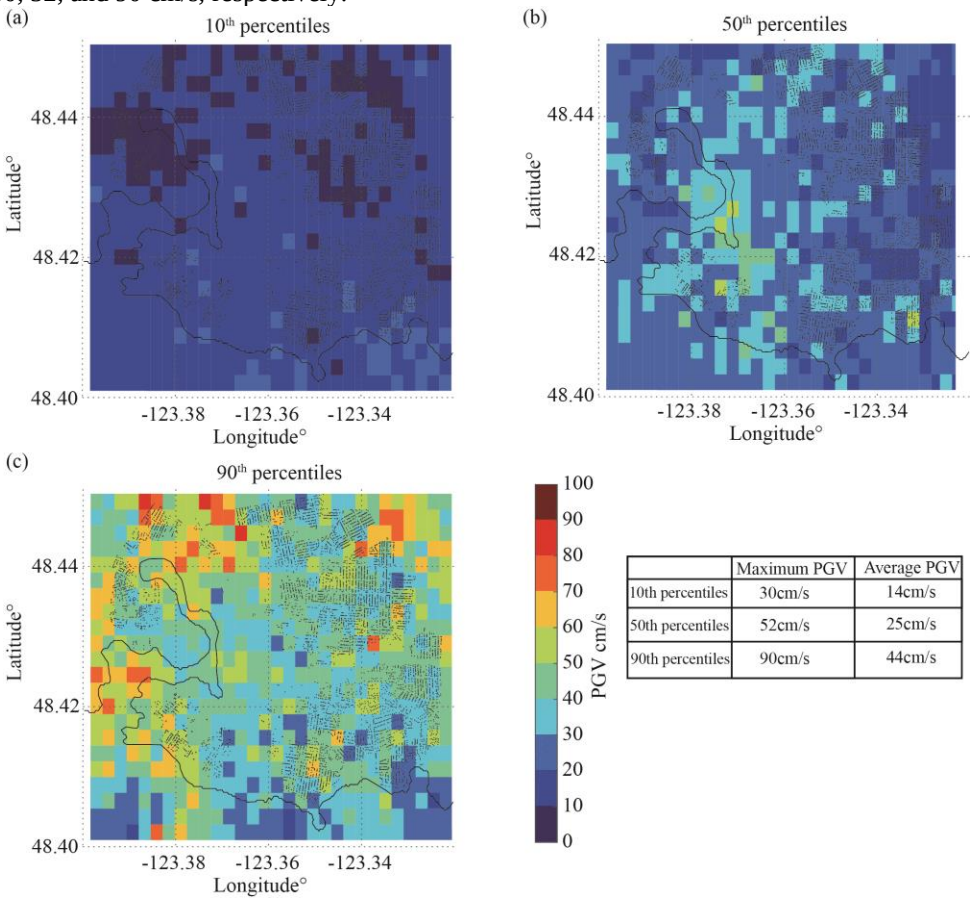

Figure 8. Mainshock shaking maps corresponding to (a) 10th, (b) 50th, and (c) 90th percentiles of the total loss.

The hazard results from **Figure 8** can be further applied to seismic risk analysis to estimate the DS of each house and the total seismic loss for the portfolio. **Figure 9**(a) shows the number of houses with DS_0, DS_1, DS_2, and DS_3 for different scenarios. The 10th percentile scenario only has 992 and 4 houses with DS_1 and DS_2, respectively, which suggest most of the houses can be immediately occupied if no major aftershocks are triggered in a short-time period. **Figure 9**(c) shows the number of houses with DS_0, DS_1, DS_2 and DS_3 for the 50th percentile scenario is 2,106, 4,394, 207, and 4, respectively. The 90th percentile scenario has a greater number of houses with DS_2 and DS_3, which

are 2,183 and 726, respectively, as indicated in **Figure 9**(e). The significantly increased number of houses with DS_3 is a result of the large PGV values with 44 cm/s on average in the 90th percentile scenario. On the other hand, **Figure 9**(b), (d), and (f) show the block maps of loss distributions corresponding to the different scenarios, which are 14, 66, and 194 million CAD$, respectively.

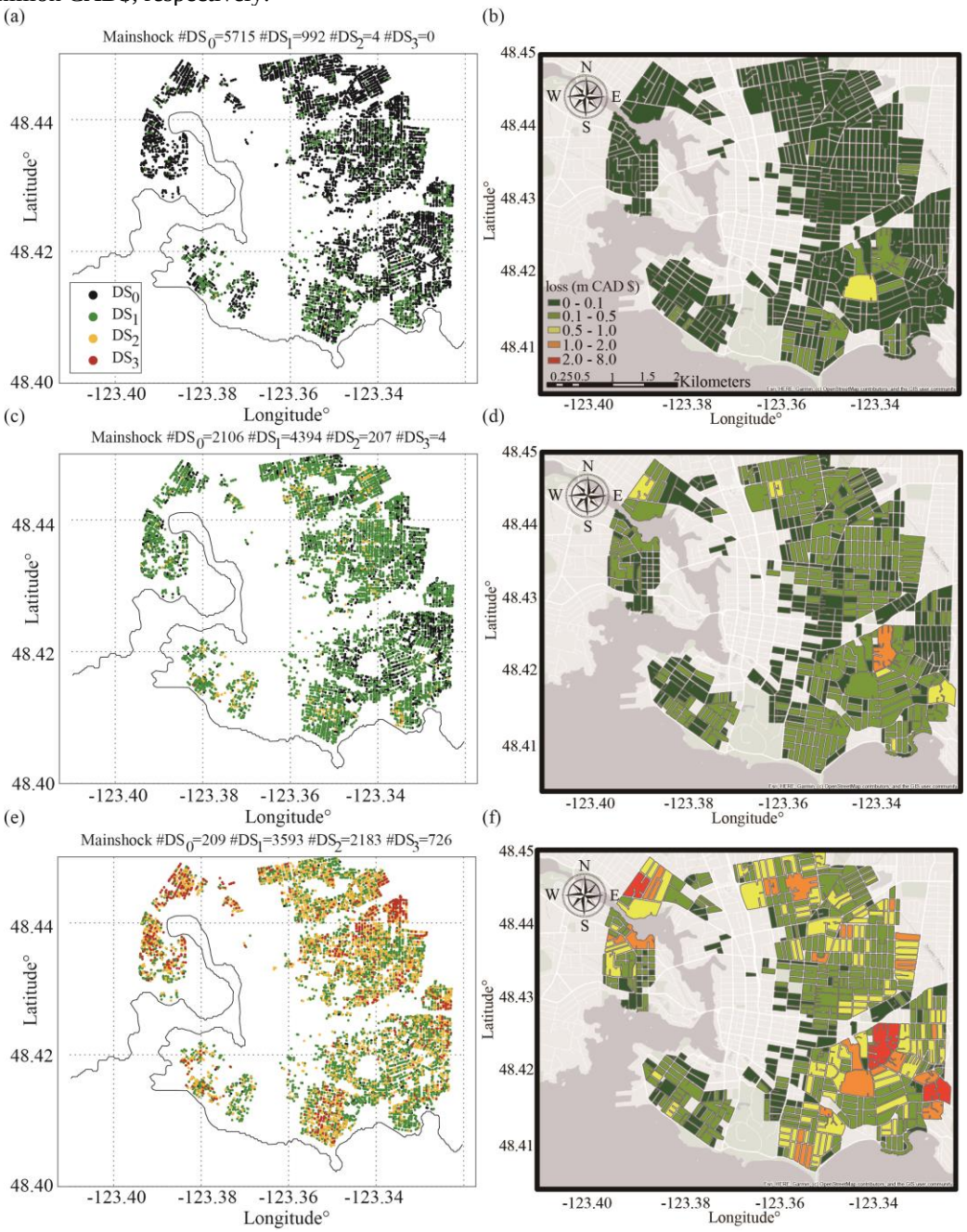

Figure 9. Simulated DS distributions of wood-frame houses for (a) 10th, (c) 50th, and (e) 90th percentiles of total losses (m CAD$) by mainshocks. The block map of seismic loss distribution of wood-frame houses for (b) 10th, (d) 50th, and (f) 90th percentile scenarios.

In the post-earthquake risk management of an M9.0 event in the CSZ, if a mainshock source model (e.g., magnitude, rupture dimensions, and strike angle) is available right after the mainshock, quasi-real-time aftershock hazard and risk assessments can be performed using the developed framework. For instance, if the 90th percentile scenario is applicable (see **Figure 8**), the aftershock forecasting can be useful to evaluate the seismic risk of critical infrastructures on day 1 (e.g., transportation system, electricity, and water supply), and ensure that the service would

be available in case of future destructive aftershocks. In addition, for the purpose of accurate building tagging, the uncertainty of the mainshock PGV can be constrained by the observed values, which is usually available right after the mainshock (e.g., USGS's ShakeMap system). This would allow reducing the uncertainty of the IM from GMPEs, and more accurate DSs of buildings can be estimated.

3.2 Impact of aftershocks on DS and loss estimation

This subsection explores the impact of aftershocks on damage probability and loss estimation of the wood-frame houses. To demonstrate the impact of aftershocks on seismic hazard and risk assessments, three single simulations within 7 days after the mainshocks corresponding to 10th, 50th, and 90th percentiles of the total loss are presented. The three cases represent different scenarios of large aftershocks for the City of Victoria: (1) distant large aftershock (10th percentile), (2) moderate-distance large aftershock (50th percentile), and (3) close large aftershock (90th percentile). Due to the large variability of mainshock PGVs from the GMPE, the mainshock PGVs for the 10th, 50th, and 90th percentiles of total losses by day 7 are selected with the similar PGVs as in **Figure 8**. This is to ensure the impact of aftershocks on risk analysis is not overestimated or underestimated due to the variability of mainshock PGVs.

Figure 10(a) shows the average damage probability of Houses 1-4 in Victoria (i.e., 6,711 buildings) for mainshocks only, and durations of 1 day, 1 week, 1 month, and 1 year after the mainshock. The impact of aftershocks on the DS of Houses 1-4 is different, noting that House 4 has a higher probability of resulting in DS_1 by the mainshocks than Houses 1-3. In comparison with the damage probability of Houses 1-4 by the mainshocks, the probabilities that damage conditions of Houses 1-4 are changed from DS_0 to DS_1 by aftershocks are 4.0%, 2.5%, 3.6%, and 2.0%, respectively. Since Houses 1-3 have higher probabilities of sustaining no damage after the mainshocks than House 4, Houses 1-3 have higher probabilities of changing from DS_0 to DS_1 due to aftershocks. Compared with the damage probability of the mainshock, additional 1.7%, 3.1%, 2.6%, and 3.8% of Houses 1-4 could change to DS_2 due to aftershocks, whereas the probabilities that aftershocks cause further damage to DS_3 are 0.3%, 0.9%, 0.7%, and 1.4%, respectively. This indicates that House 4 damaged by the mainshocks tends to have further damage to change to DS_2 and DS_3. The higher damage probability of DS_3 for House 4 suggests that the retrofitting of House 4 to meet the seismic provisions of the National Building Code of Canada (Houses 1 or 2) might be necessary to reduce the probability of demolition and reconstruction of House 4 after M9.0 sequences.

The loss exceedance curves of mainshock-aftershock sequences for mainshocks only, and durations of 1 day, 1 week, 1 month, and 1 year are shown in **Figure 10**(b). The 10th, 50th, and 90th percentiles of total aggregated losses by day 7 are 20, 71, and 224 million CAD$, respectively. On average, aftershocks could cause additional 10% and 20% losses after 1 week and 1 year of the mainshock, respectively, in comparison with the loss exceedance curves of the mainshocks. The effects of aftershocks on seismic loss estimation are consistent with other studies (e.g., [20]).

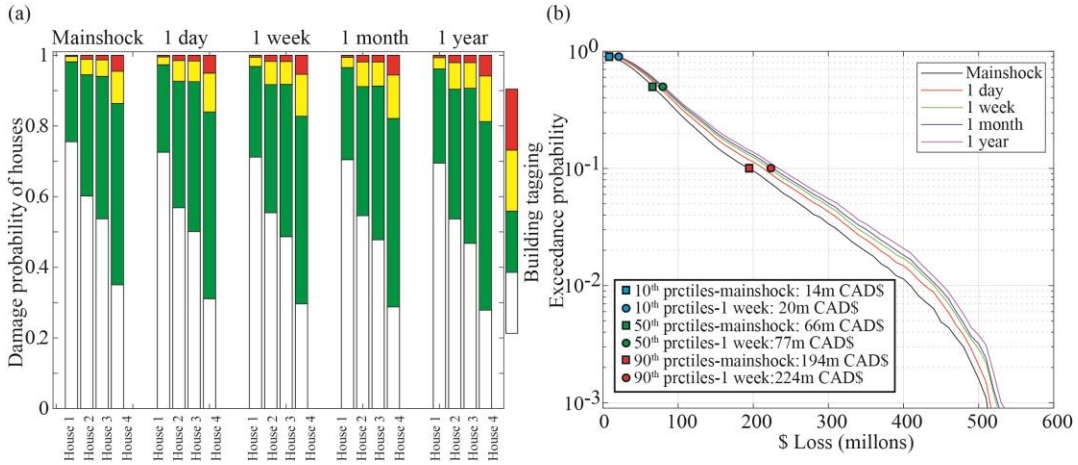

Figure 10. (a) Damage probability of Houses 1-4 and (b) loss exceedance curves of mainshock-aftershock sequences at durations of 1 day, 1 week, 1 month, and 1 year based on 6,711 houses in Victoria. 10th, 50th, and 90th percentiles of aggregated losses by mainshock-aftershocks within 1 week are 20, 77, and 224 million CAD$, respectively.

To illustrate different scenarios for risk management decisions, the seismic hazard and risk results within 7 days after the mainshocks corresponding to 10th, 50th, and 90th percentiles of the total loss are examined. **Figure 11** shows plots of three single simulations of aftershock epicentres and latitudinal distribution of aftershocks up to day 7 after the mainshock corresponding to the 10th, 50th, and 90th percentiles of total losses from 10,000 simulations. These

three scenarios represent (1) a distant large aftershock (10th percentile in **Figure 11**(a) and (b)), (2) a moderate-distance large aftershock (50th percentile in **Figure 11**(c) and (d)), and (3) a closer large aftershock (90th percentile in **Figure 11**(e) and (f)) of M7.0-class aftershocks. In comparison with the distant M7.0-class aftershocks from 10th and 50th percentile scenarios, the M7.2 subduction aftershock (48.49°N, 124.69°W) in the 90th percentile scenario in **Figure 11**(e) is much closer to Victoria and may cause higher seismic losses.

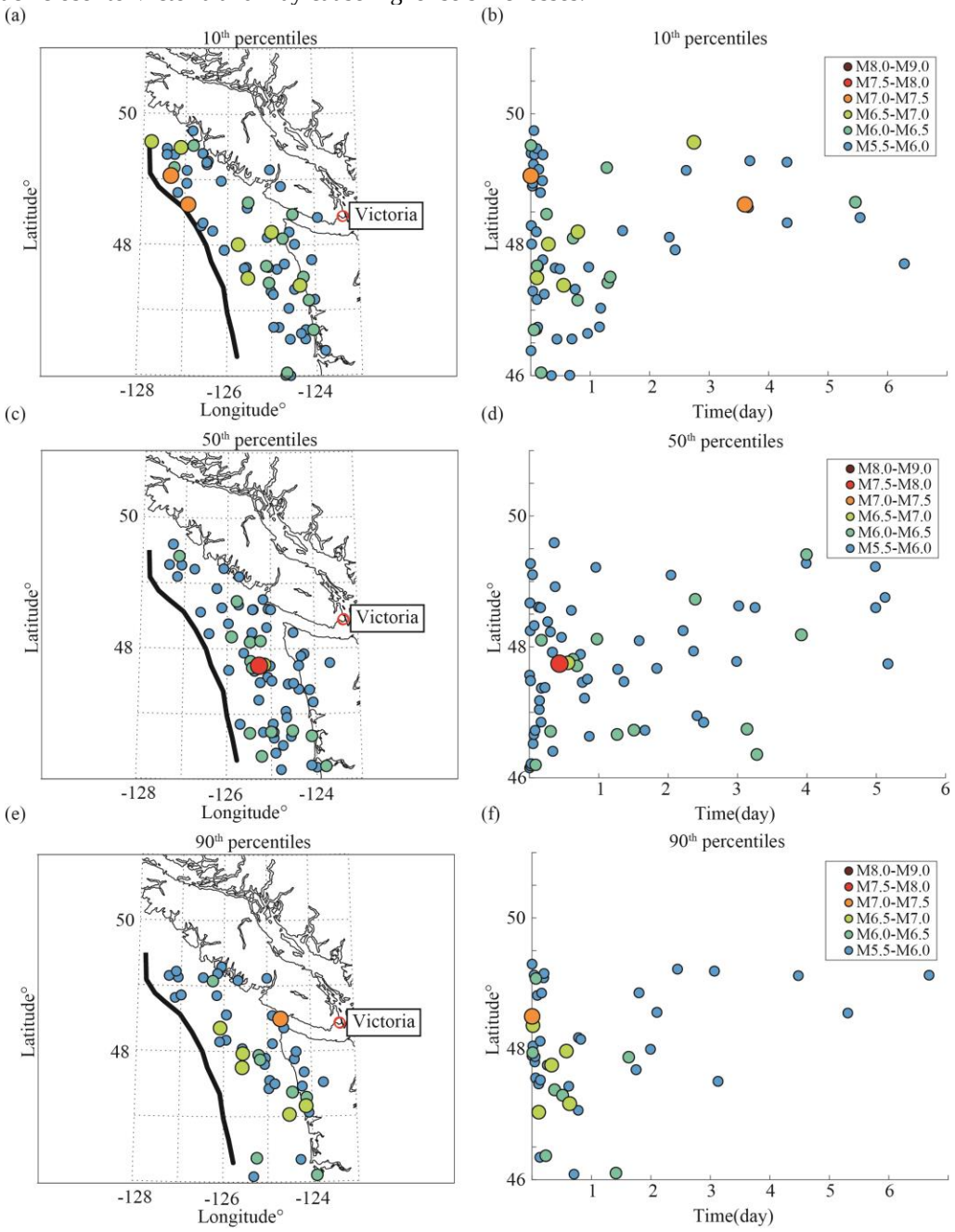

Figure 11. Aftershock epicentres and latitudinal distribution of aftershocks with time on day 7 after the mainshock corresponding to (a, b) 10th percentiles, (c, d) 50th percentiles, and (e, f) 90th percentiles of the total loss.

Figure 12 shows three single simulations of the mainshock PGV maps and the maximum aftershock PGV maps corresponding to the seismicity plots in **Figure 11**. The same ranges of the maximum and average mainshock PGVs are selected in **Figure 12**(a), (c), and (e) as in **Figure 8** to facilitate the visual comparison. Although two M7-class events from the 10th percentile scenario are triggered in the offshore region as shown in **Figure 11**(a), their impacts on the ground motion hazard are limited due to the long rupture distances. No large aftershocks are triggered

near Victoria (e.g., within 50 km); therefore, only a few patches in the maximum aftershock PGV map by day 7 have PGV values larger than 10 cm/s in **Figure 12**(b). Although the epicentre of the M7.8 aftershock (47.74°N, 125,27°W) from the 50th percentile scenario is 200 km away from Victoria, the rupture distance is 110 km when a large finite fault plane is accounted for based on the scaling law of fault dimensions [31] and some sites in the east of Victoria have PGV values larger than 10 cm/s in **Figure 12**(d). The impact of the M7.2 event from the 90th percentile scenario on the hazard map in **Figure 12**(f) is significant. The majority of the maximum aftershock PGV values exceeds 10 cm/s almost everywhere across the City of Victoria.

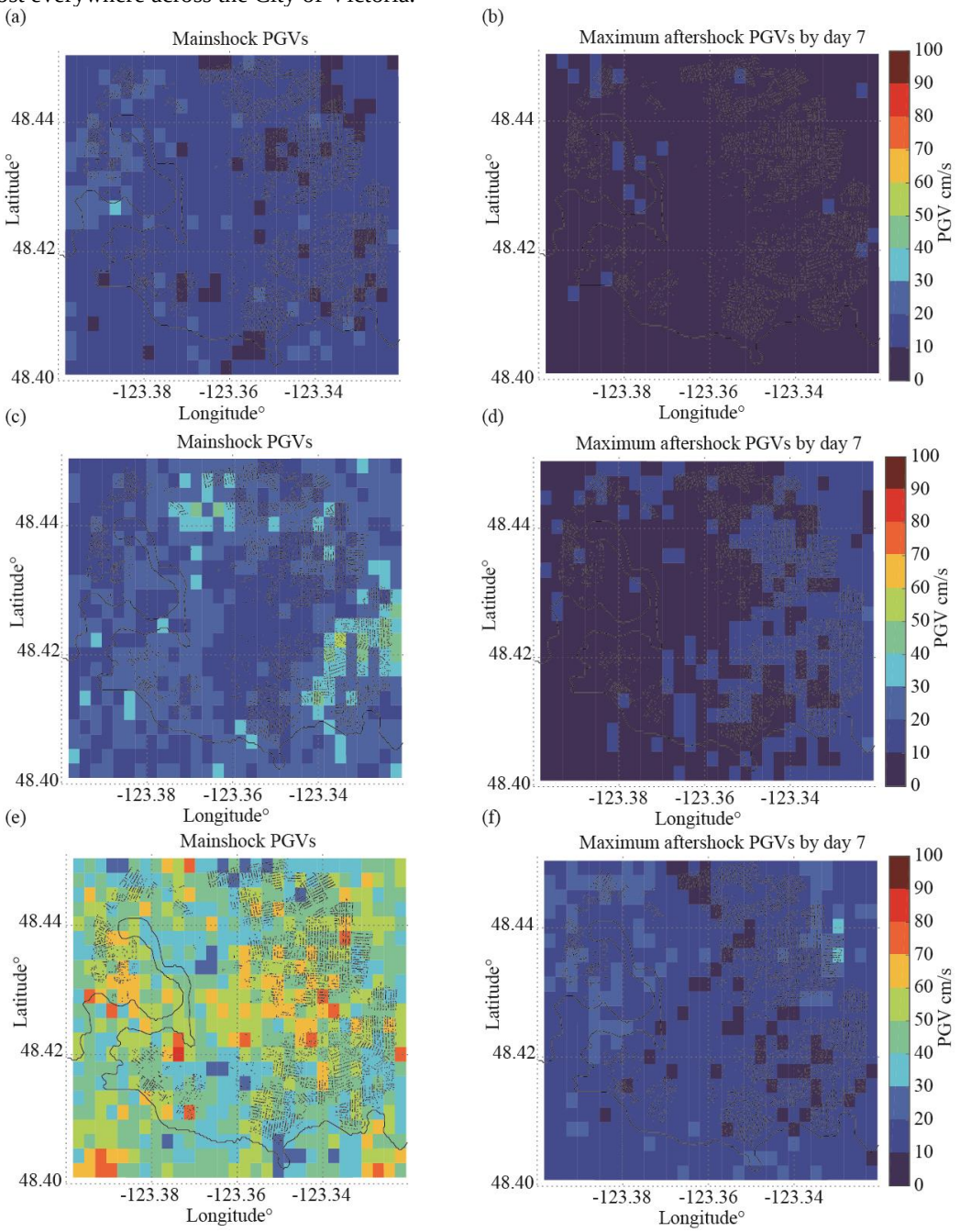

Figure 12. Mainshock PGV map and maximum aftershock PGV hazard map by day 7 for the City of Victoria corresponding to (a, b) 10th percentiles, (c, d) 50th percentiles, and (e, f) 90th percentiles of the total loss.

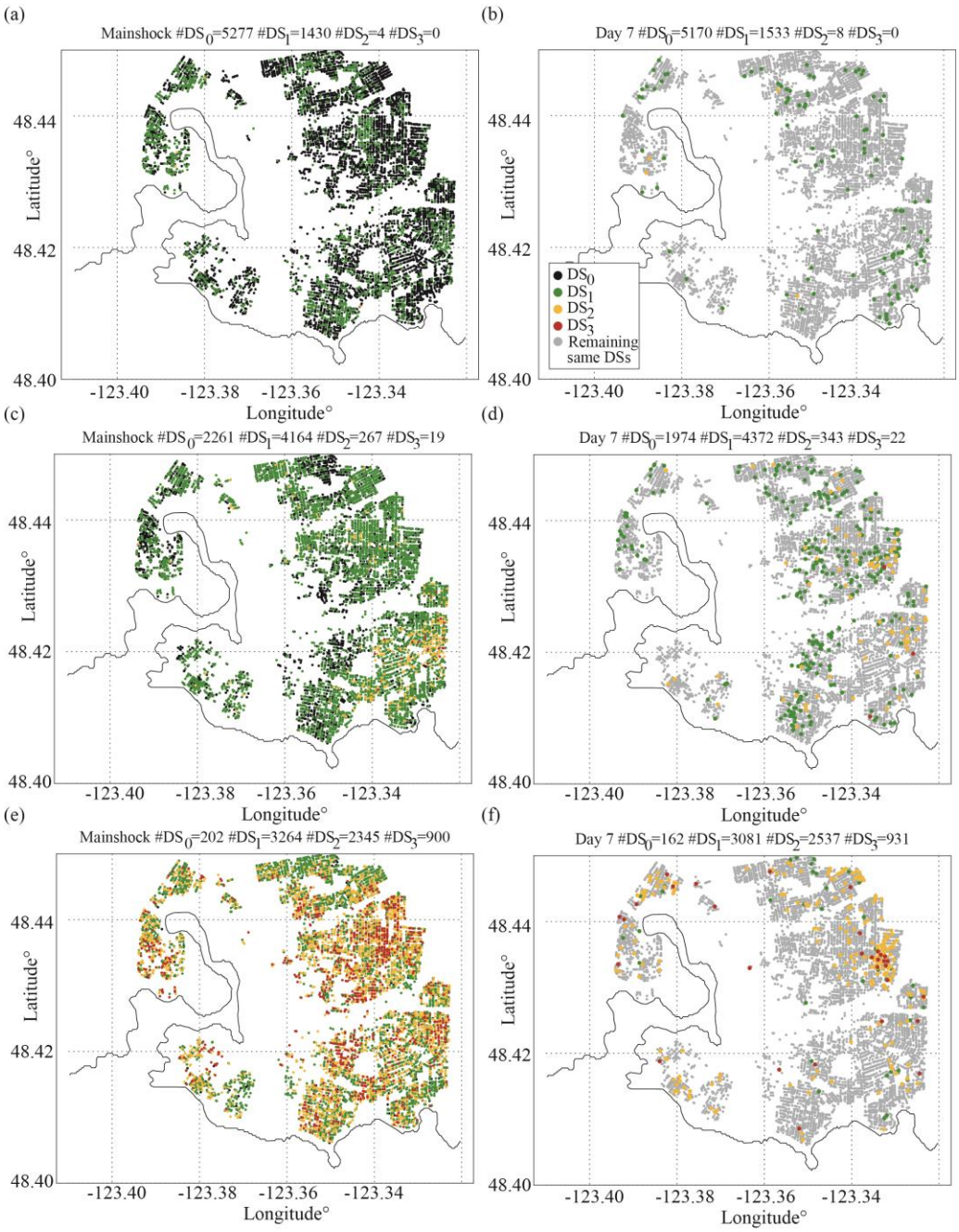

Figure 13. DS distributions of wood-frame houses due to the mainshock (left panels) and additional damage to the aftershock sequence within 1 week (right panels) corresponding to (a, b) 10th percentiles, (c, d) 50th percentiles, and (e, f) 90th percentiles of the total loss.

The DS distributions of wood-frame houses by mainshock and mainshock-aftershock sequences on day 7 are shown in **Figure 13**. For the 10th percentile scenario, the number of houses with DS_1 and DS_2, respectively, is increased by 103 and 4, due to aftershocks within 7 days after the mainshock. The aftershocks from the 10th percentile scenario contribute to a few patches on the aftershock hazard map with PGV > 10 cm/s in **Figure 12**(b), which could not cause significant damage to houses. Most of the houses would remain intact or experience minor damage (DS_1). In terms of the 50th percentile scenario, the M7.5-class event causes some moderate damage to the houses in Victoria. From **Figure 13**(c) and (d), the number of houses with DS_1, DS_2, and DS_3 due to the mainshock is 4,164, 267, and 19, respectively. After one week, the numbers of houses with DS_1, DS_2, and DS_3 increase to 4,372, 343, and 22, respectively. More houses are changed to DS_2 in the eastern part of Victoria, which is consistent with the aftershock

hazard map in **Figure 12**(d). The impact of the M7.0-class event from the 90th percentile scenario on the seismic risk assessment is substantial. The number of houses with DS_1, DS_2, and DS_3 by the mainshock is 3,264, 2,345, and 900, respectively. After one week of the mainshock, due to the M7.2 aftershock, the number of houses with DS_1, DS_2, and DS_3 is 3,081, 2,537, and 931, respectively.

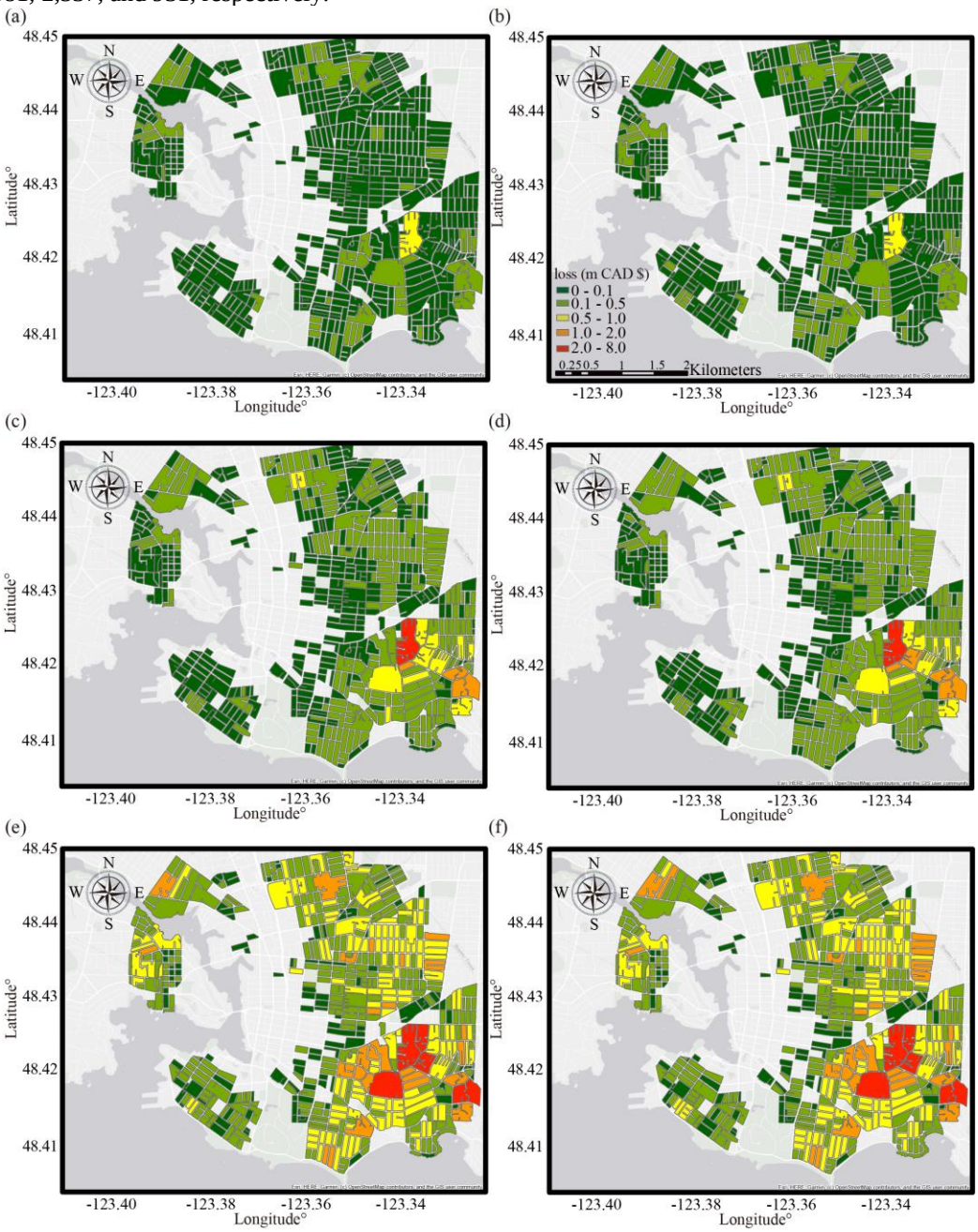

Figure 14. Seismic loss distribution of wood-frame houses due to the mainshock (left panels) and additional damage to the aftershock sequence within 1 week (right panels) corresponding to (a, b) 10th percentiles, (c, d) 50th percentiles, and (e, f) 90th percentiles of the total loss.

Figure 14 shows the block map of seismic loss distributions of wood-frame houses in the City of Victoria by mainshock and the mainshock-aftershock sequence up to day 7. In total, the aggregate seismic loss of the 10th percentile case shown in **Figure 13**(a) and (b) is increased from 18 to 20 million CAD$. The aggregate losses of the 50th percentile case from **Figure 13**(c) and (d) are increased from 71 to 77 million CAD$. For the 90th percentile case,

the aggregate loss is increased by 9 million CAD$ in **Figure 13**(f) in comparison with 215 million CAD$ for the mainshock alone.

For the post-earthquake risk management of M9.0 events, after 1 week of the mainshock, the quasi-real-time aftershock hazard and risk assessments in **Figures 12-14** can be helpful for the building tagging and inspection of wood-frame houses, assuming the seismic vulnerability models for residential houses are applicable. For example, the output of the framework can provide the probability distribution of the DSs on the day of the inspection for building tagging and daily forecasts of the DSs in a short-time period after the inspection day. This can be part of building inspection along with conventional building tagging [46] to provide additional information for structural inspectors.

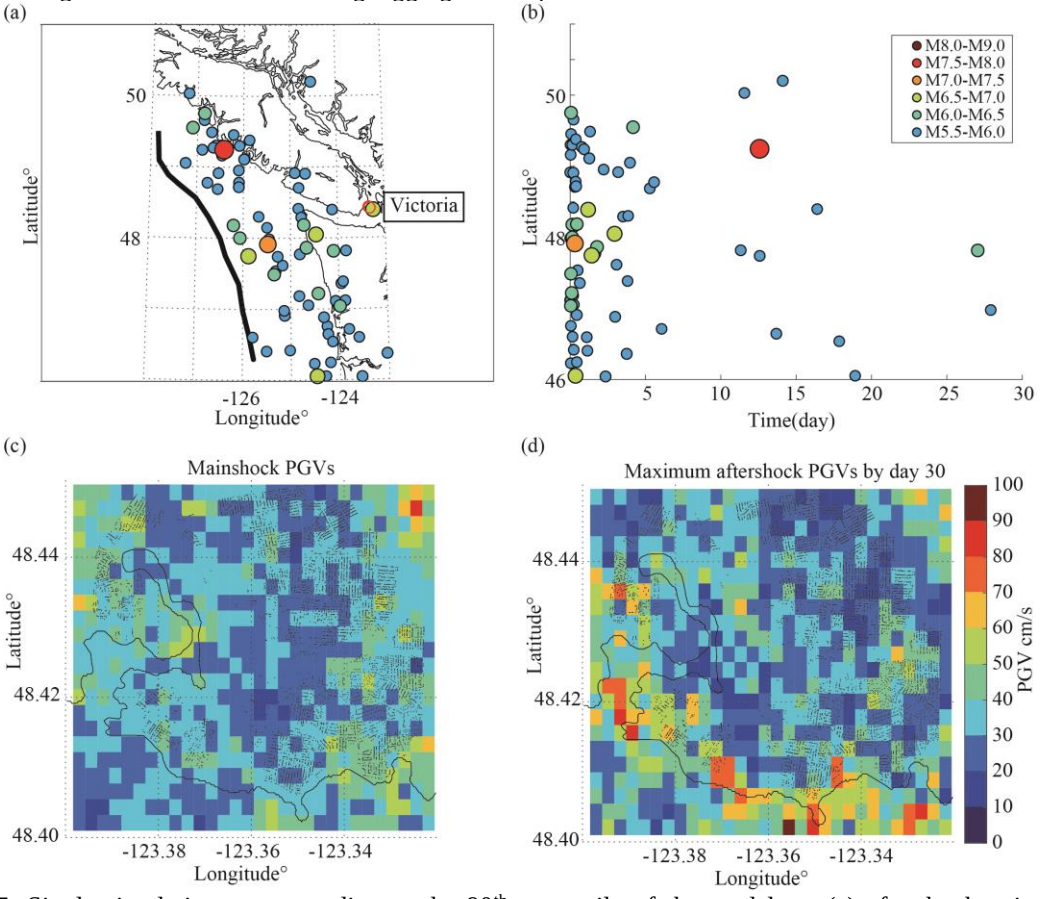

Figure 15. Single simulation corresponding to the 90th percentile of the total loss: (a) aftershock epicentres, (b) latitudinal distribution of aftershocks with time to day 30 after the mainshock, (c) mainshock hazard map, and (d) the maximum aftershock hazard map within 30 days after the mainshock for the City of Victoria.

3.3 Extreme case with a triggered crustal aftershock near Victoria

A more destructive crustal aftershock case is presented as a worst scenario. An example of the 90th percentiles of total losses within one month after the mainshock is shown in **Figure 15**. To show the potential impact of destructive aftershocks on hazard and risk assessment for the City of Victoria, a single simulation with a lower maximum mainshock PGV is considered (81 cm/s) in **Figure 15**(c), compared with 90 cm/s in the 90th percentile of the mainshocks simulations in **Figure 8**. An M6.5 aftershock is triggered near Victoria, which is a shallow crustal aftershock (48.39°N, 123.24°W) with a rupture distance less than 10 km to Victoria. The maximum aftershock PGV values in **Figure 15**(d) are contributed by the triggered shallow crustal event. This type of shallow crustal event has been previously identified as potentially damaging scenarios near Victoria in past studies, for example, the Leech River Valley fault-M6.0 event and the Devil's Mountain fault-M7.5 event [40,47].

In **Figure 16**, due to the triggered crustal event, the number of houses with DS_2 and DS_3 increased by 2,213 and 440, respectively. Less than 10% of the houses remain in DS_0. The aggregate losses are increased by 108 million CAD$ in comparison with 121 million CAD$ due to the mainshock. The losses due to the aftershocks are almost the same amount as those due to the mainshock.

The 90th percentile scenarios for different durations (1 week and 1 month) suggest that the impact of destructive aftershocks on seismic risk assessment could be moderate events (e.g., an M6.0-class crustal event) with short rupture distances in the shallow crust or large events (e.g., an M7.5-class subduction-zone event) with greater rupture distances on the subduction-zone interface. The examples of the large M7.2 subduction-zone aftershock in **Section 3.2** and the shallow crustal event with the shortest rupture distance of less than 10 km to Victoria in this section demonstrate the potential impact of destructive aftershocks on a municipality-wide risk assessment.

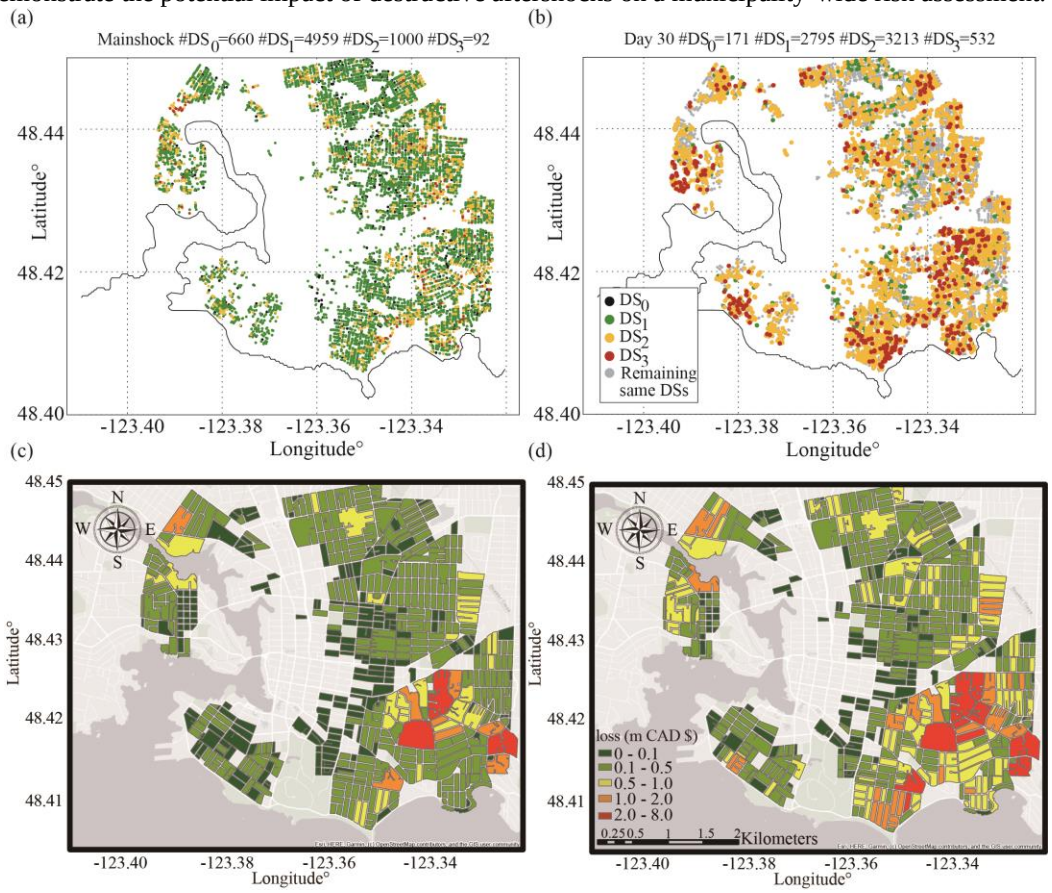

Figure 16. DS distribution of wood-frame houses for 90th percentiles of the total loss by (a) mainshock and (b) mainshock-aftershock sequences on day 30. The block map of seismic loss distribution of wood-frame houses in the City of Victoria by (c) mainshock and (d) mainshock-aftershock sequence on day 30.

4 CONCLUSIONS

This study developed a new simulation framework to assess spatiotemporal seismic hazard and risk due to M9.0 mainshock-aftershock sequences using a realistic building portfolio of wood-frame houses for Victoria, BC, Canada. The ETAS simulation from Zhang *et al.* [15] with the suggested ETAS parameters from Zhang *et al.* [16] was applied to generate stochastic M9.0 earthquake sequences for the CSZ. Applicable GMPEs were selected for the CSZ to calculate the time-dependent hazard results at multiple sites accounting for spatial correlations of ground motions. The hazard results were further applied to state-dependent fragility models to assess the spatiotemporal risk to multiple wood-frame houses in the City of Victoria, BC, Canada.

The results showed that the impact of the variability of mainshock PGVs on total loss is significant. The 10th, 50th, and 90th percentiles of total mainshock loss (corresponding to the average mainshock PGV values with 14 cm/s, 25 cm/s, and 44 cm/s) are 14, 66, and 194 million CAD$, respectively. On average, aftershocks could cause additional 10% and 20% losses after 1 week and 1 year of the mainshock, respectively. Single simulations of mainshock-aftershock results show that the developed simulation framework can capture the subduction and crustal aftershock rates in space and time and further estimate the DS and loss distributions for risk management decisions. Destructive aftershocks could be triggered by M9.0 events. Occurrence of an M6.0-class crustal event or an M7.5-class subduction-zone event could lead to 90th percentiles of the total loss. If the mainshock source model is available right after the mainshock, this framework can facilitate the quasi-real-time aftershock hazard and risk assessments.

The limitations of this study include: (1) for more accurate hazard estimates, a high-resolution V_{s30} map is necessary; (2) other GMPEs for subduction-zone events that use PGV as the output and include M9.0 observed records need to be considered; and (3) accurate loss estimations (considering different EDPs for structural and non-structural components) would require state-dependent fragility curves that are applicable to other structure types, which are beyond the scope of this study.

ACKNOWLEDGEMENTS

For this work, K.G. received funding from the Canada Research Chair program (950-232015) and the NSERC Discovery Grant (RGPIN-2019-05898), and M.J.W. received funding from the European Union's Horizon 2020 research and innovation program (No 821115, RISE: Real-Time Earthquake Risk Reduction for a Resilient Europe). L.Z. and M.J.W. appreciate the support from the London Mathematical Laboratory (http://lml.org.uk/). M.J.W. was also supported by the Southern California Earthquake Center (No. 10013); SCEC is funded by NSF Cooperative Agreement EAR-1600087 & USGS Cooperative Agreement G17AC00047.

REFERENCES

1. Hirose F, Miyaoka K, Hayashimoto N, Yamazaki T, Nakamura M. Outline of the 2011 off the Pacific coast of Tohoku earthquake (Mw 9.0)—seismicity: foreshocks, mainshock, aftershocks, and induced activity—. *Earth, Planets and Space* 2011; **63**(7): 513–518.
2. Goda K, Pomonis A, Chian SC, Offord M, Saito K, Sammonds P, *et al.* Ground motion characteristics and shaking damage of the 11th March 2011 M w 9.0 Great East Japan earthquake. *Bulletin of Earthquake Engineering* 2013; **11**(1): 141–170.
3. Nazari N, Van De Lindt JW, Li Y. Effect of mainshock-aftershock sequences on woodframe building damage fragilities. *Journal of Performance of Constructed Facilities* 2013; **29**(1). DOI: 10.1061/(ASCE)CF.1943- 5509.0000512.
4. Ebrahimian H, Jalayer F, Asprone D, Lombardi AM, Marzocchi W, Prota A, *et al.* A performance-based framework for adaptive seismic aftershock risk assessment. *Earthquake Engineering & Structural Dynamics* 2014; **43**(14): 2179–2197.
5. Iervolino I, Giorgio M, Chioccarelli E. Closed-form aftershock reliability of damage-cumulating elastic-perfectly-plastic systems. *Earthquake Engineering & Structural Dynamics* 2014; **43**(4): 613–625.
6. Field EH, Jordan TH, Jones LM, Michael AJ, Blanpied ML, others. The potential uses of operational earthquake forecasting. *Seismological Research Letters* 2016; **87**(2A): 313–322.
7. Jordan TH, Jones LM. Operational earthquake forecasting: some thoughts on why and how. *Seismological Research Letters* 2010; **81**(4): 571–574.
8. Goldfinger C, Nelson CH, Morey a. E, Joel E J, Patton J, Karabanov E, *et al.* Turbidite event history — methods and implications for holocene paleoseismicity of the Cascadia Subduction Zone. *US Geological Survey Professional Paper 1661-F* 2012: 170 p.
9. Satake K, Shimazaki K, Tsuji Y, Ueda K. Time and size of a giant earthquake in Cascadia inferred from Japanese tsunami records of January 1700. *Nature* 1996; **379**(6562): 246–249.
10. Ventura CE, Finn WDL, Onur T, Blanquera A, Rezai M. Regional seismic risk in British Columbia : classification of buildings and development of damage probability functions. *Canadian Journal of Civil Engineering* 2005; **32**(2): 372–387.
11. Onur T, Ventura CE, Finn WDL. Regional seismic risk in British Columbia—damage and loss distribution in Victoria and Vancouver. *Canadian Journal of Civil Engineering* 2005; **32**(2): 361–371.
12. Ogata Y. Space-time point-process models for earthquake occurrences. *Annals of the Institute of Statistical Mathematics* 1998; **50**(2): 379–402.
13. Iervolino I, Chioccarelli E, Giorgio M, Marzocchi W, Zuccaro G, Dolce M, *et al.* Operational (short-term) earthquake loss forecasting in Italy. *Bulletin of the Seismological Society of America* 2015; **105**(4): 2286–2298.
14. Field E, Porter K, Milner K. A prototype operational earthquake loss model for California based on UCERF3-ETAS--a first look at valuation. *Earthquake Spectra* 2017; **33**(4): 1279–1299.
15. Zhang L, Werner MJ, Goda K. Spatiotemporal seismic hazard and risk assessment of aftershocks of M 9 megathrust earthquakes. *Bulletin of the Seismological Society of America* 2018; **108**(6): 3313–3335.
16. Zhang L, Werner MJ, Goda K. Variability of ETAS parameters in global subduction zones and applications to mainshock-aftershock hazard assessment. *Bulletin of the Seismological Society of America* 2020; **110**(1): 191–212.
17. Tesfamariam S, Goda K. Loss estimation for non-ductile reinforced concrete building in Victoria, British

Columbia, Canada: effects of mega-thrust Mw9-class subduction earthquakes and aftershocks. *Earthquake Engineering & Structural Dynamics* 2015; **44**(13): 2303–2320.
18. Koduru SD, Haukaas T. Probabilistic seismic loss assessment of a Vancouver high-rise building. *Journal of Structural Engineering* 2010; **136**(3): 235–245.
19. Goda K, Atkinson GM. Seismic performance of wood-frame houses in south-western British Columbia. *Earthquake Engineering & Structural Dynamics* 2011; **40**(8): 903–924.
20. Salami MR, Goda K. Seismic loss estimation of residential wood-frame buildings in southwestern British Columbia considering mainshock-aftershock sequences. *Journal of Performance of Constructed Facilities* 2014; **28**(6). DOI: 10.1061/(ASCE)CF.1943-5509.0000514.
21. Goda K, Atkinson GM, Hong HP. Seismic loss estimation of wood-frame houses in south-western British Columbia. *Structural Safety* 2011; **33**(2): 123–135.
22. Goda K, Hong HP. Estimation of seismic loss for spatially distributed buildings. *Earthquake Spectra* 2008; **24**(4): 889–910.
23. Zhang L, Goda K, De Luca F, De Risi R. Mainshock-aftershock state-dependent fragility curves: the case of wood-frame houses in British Columbia, Canada. *Earthquake Engineering & Structural Dynamics* 2020. DOI: 10.1002/eqe.3269.
24. Halchuk S, Allen TI, Rogers GC, Adams J. Seismic hazard earthquake epicentre file (SHEEF2010) used in the fifth generation seismic hazard maps of Canada. *Geological Survey of Canada Open File* 2015; **7724**. DOI: 10.4095/296908.
25. Petersen MD, Moschetti MP, Powers PM, Mueller CS, Haller KM, Frankel AD, *et al.* Documentation for the 2014 update of the United States national seismic hazard maps. *US Geological Survey Open-File Report* 2014: 243 p. DOI: 10.3133/ofr20141091.
26. Wang K, Wells R, Mazzotti S, Hyndman RD, Sagiya T. A revised dislocation model of interseismic deformation of the Cascadia subduction zone. *Journal of Geophysical Research: Solid Earth* 2003; **108**. DOI: 10.1029/2001JB001227.
27. Flück P, Hyndman RD, Wang K. Three-dimensional dislocation model for great earthquakes of the Cascadia subduction zone. *Journal of Geophysical Research: Solid Earth* 1997; **102**(B9): 20539–20550.
28. Hyndman RD. Downdip landward limit of Cascadia great earthquake rupture. *Journal of Geophysical Research: Solid Earth* 2013; **118**(10): 5530–5549.
29. Storesund R, Dengler L, Mahin S, Collins BD, Hanshaw M, Turner F, *et al.* M 6.5 Earthquake Offshore Northern California January 9, 2010. *GEER Field Reconnaissance Summary* 2010.
30. Wang K, Tréhu AM. Invited review paper: some outstanding issues in the study of great megathrust earthquakes—The Cascadia example. *Journal of Geodynamics* 2016; **98**: 1–18.
31. Thingbaijam KKS, Martin Mai P, Goda K. New empirical earthquake-source scaling laws. *Bulletin of the Seismological Society of America* 2017; **107**(5): 2225–2246.
32. Hayes GP, Wald DJ, Johnson RL. Slab1.0: a three-dimensional model of global subduction zone geometries. *Journal of Geophysical Research: Solid Earth* 2012; **117**(B1). DOI: 10.1029/2011JB008524.
33. Power JA, Lahr JC, Page RA, Chouet BA, Stephens CD, Harlow DH, *et al.* Seismic evolution of the 1989--1990 eruption sequence of Redoubt Volcano, Alaska. *Journal of Volcanology and Geothermal Research* 1994; **62**(1–4): 69–94.
34. Ghofrani H, Atkinson GM. Ground-motion prediction equations for interface earthquakes of M7 to M9 based on empirical data from Japan. *Bulletin of Earthquake Engineering* 2014; **12**(2): 549–571.
35. Boore DM, Stewart JP, Seyhan E, Atkinson GM. NGA-West2 equations for predicting PGA, PGV, and 5% damped PSA for shallow crustal earthquakes. *Earthquake Spectra* 2014; **30**(3): 1057–1085.
36. Zhao JX, Zhang J, Asano A, Ohno Y, Oouchi T, Takahashi T, *et al.* Attenuation relations of strong ground motion in Japan using site classification based on predominant period. *Bulletin of the Seismological Society of America* 2006; **96**(3): 898–913.
37. Atkinson GM, Boore DM. Empirical ground-motion relations for subduction-zone earthquakes and their application to Cascadia and other regions. *Bulletin of the Seismological Society of America* 2003; **93**(4): 1703–1729.
38. Abrahamson N, Gregor N, Addo K. BC Hydro ground motion prediction equations for subduction earthquakes. *Earthquake Spectra* 2016; **32**(1): 23–44.
39. Zhao JX, Liang X, Jiang F, Xing H, Zhu M, Hou R, *et al.* Ground-motion prediction equations for subduction interface earthquakes in Japan using site class and simple geometric attenuation functions. *Bulletin of the Seismological Society of America* 2016; **106**(4): 1518–1534.
40. Morell KD, Regalla C, Leonard LJ, Amos C, Levson V. Quaternary rupture of a crustal fault beneath

Victoria, British Columbia, Canada. *GSA Today* 2017; **27**. DOI: 10.1130/GSATG291A.1.
41. Wald DJ, Allen TI. Topographic slope as a proxy for seismic site conditions and amplification. *Bulletin of the Seismological Society of America* 2007; **97**(5): 1379–1395.
42. Monahan PA, Levson VM. Development of a shear wave velocity model of the near-surface deposits of Southwestern British Columbia, Canada. *International Conferences on Recent Advances in Geotechnical Earthquake Engineering and Soil Dynamics* 2001.
43. Goda K, Hong HP. Spatial correlation of peak ground motions and response spectra. *Bulletin of the Seismological Society of America* 2008; **98**(1): 354–365.
44. Goda K, Atkinson GM. Intraevent spatial correlation of ground-motion parameters using SK-net data. *Bulletin of the Seismological Society of America* 2010; **100**(6): 3055–3067.
45. White TW, Ventura CE. Seismic performance of wood-frame residential construction in British Columbia-technical report. *Earthquake Eng. Research Facility Report No. 06-03*, University of British Columbia, Vancouver, Canada, 2006.
46. Bazzurro P, Cornell CA, Menun C, Motahari M. Guidelines for seismic assessment of damaged buildings. *13th World Conference on Earthquake Engineering*, 2004.
47. Personius SF, Briggs RW, Nelson AR, Schermer ER, Maharrey JZ, Sherrod BL, *et al.* Holocene earthquakes and right-lateral slip on the left-lateral Darrington--Devils Mountain fault zone, northern Puget Sound, Washington. *Geosphere* 2014; **10**(6): 1482–1500.